BioOne COMPLETE

RITCARD: Radiation-Induced Tracks, Chromosome Aberrations, Repair and Damage

Authors: Plante, Ianik, Ponomarev, Artem, Patel, Zarana, Slaba, Tony, and Hada, Megumi

Source: Radiation Research, 192(3) : 282-298

Published By: Radiation Research Society

URL: https://doi.org/10.1667/RR15250.1

BioOne Complete (complete.BioOne.org) is a full-text database of 200 subscribed and open-access titles in the biological, ecological, and environmental sciences published by nonprofit societies, associations, museums, institutions, and presses.

Your use of this PDF, the BioOne Complete website, and all posted and associated content indicates your acceptance of BioOne's Terms of Use, available at www.bioone.org/terms-of-use.

Usage of BioOne Complete content is strictly limited to personal, educational, and non - commercial use. Commercial inquiries or rights and permissions requests should be directed to the individual publisher as copyright holder.

BioOne sees sustainable scholarly publishing as an inherently collaborative enterprise connecting authors, nonprofit publishers, academic institutions, research libraries, and research funders in the common goal of maximizing access to critical research.

Downloaded From: https://bioone.org/journals/Radiation-Research on 02 May 2024
Terms of Use: https://bioone.org/terms-of-use

RADIATION RESEARCH **192**, 282–298 (2019)
0033-7587/19 $15.00
©2019 by Radiation Research Society.
All rights of reproduction in any form reserved.
DOI: 10.1667/RR15250.1

RITCARD: Radiation-Induced Tracks, Chromosome Aberrations, Repair and Damage

Ianik Plante,[a,1] Artem Ponomarev,[a] Zarana Patel,[a] Tony Slaba[b] and Megumi Hada[c]

[a] *KBRWyle, Houston, Texas 77058;* [b] *NASA Langley Research Center, Hampton, Virginia 23681; and* [c] *Prairie View A&M University, Prairie View, Texas 77446*

Plante, I., Ponomarev, A., Patel, Z., Slaba, T. and Hada, M. RITCARD: Radiation-Induced Tracks, Chromosome Aberrations, Repair and Damage. *Radiat. Res.* 192, 282–298 (2019).

Chromosome aberrations (CAs) are one of the effects of radiation exposure and can have implications for human health in the space environment, since they are related to cancer risk. In radiation research, chromosome aberrations are a convenient biomarker for carcinogenesis. To shed light on the formation and quality of chromosome aberrations in the space environment, many experiments and simulations have been performed using chromosome aberrations in human cells, induced by heavy ions, which are present in galactic cosmic rays (GCRs). In this work, the new simulation program, radiation-induced tracks, chromosome aberrations, repair and damage (RITCARD), is presented. This software program is based on the algorithm used in the NASA Radiation Track Image (NASARTI) model with some improvements. NASARTI and RITCARD are both comprised of four parts: a random walk (RW) algorithm for simulating chromosomes in a nucleus; a deoxyribonucleic acid (DNA) damage algorithm; a break repair process; and a function to assess and count chromosome aberrations. Prior to running RITCARD, the code, relativistic ion tracks (RITRACKS), is used to simulate detailed radiation track structure and calculate time-dependent differential voxel dose maps in a parallelepiped centered on a cell nucleus. The RITCARD program reads the pre-calculated voxel dose and locates the intersections between the voxels and the chromosomes that were simulated by random walk. Radiation-induced breaks occur strictly at these intersections with a probability that is a function of the voxel dose. When a break occurs in the random walk, the corresponding chromosome piece is cut into two fragments where each has a free end at the position of the break. RITCARD generates a collection of all fragments, free ends, and enlists free end pairs. In the next step, the algorithm simulates the time-dependent rejoining of free end pairs, using different probabilities for pairs originating from a given break (proper) or from different breaks (improper), which results in the formation of fragment sequences. By grouping these sequences, the program determines the number and types of aberrations, based on the same criteria used in our experiment. The new program is used to assess the yields of various types of chromosome aberrations in human fibroblast cells for several ions ($^{1}H^{+}$, $^{4}He^{2+}$, $^{12}C^{6+}$, $^{16}O^{8+}$, $^{20}Ne^{10+}$, $^{28}Si^{14+}$, $^{48}Ti^{22+}$ and $^{56}Fe^{26+}$) with energies varying from 10 to 1,000 MeV/n. The results show linear and linear-quadratic dose dependence for most chromosome aberrations types. The calculation results were compared with those obtained by fluorescence *in situ* hybridization (FISH) experiments that were performed by our group. The simulations and experiments are in better agreement at lower LET. Regarding the simulation results, the coefficient of the linear part of the dose-dependence curve also peaks at an LET value of approximately 100 keV/μm, which evokes a relative biological effectiveness (RBE) peak found by other researchers. © 2019 by Radiation Research Society

INTRODUCTION

Radiation poses a hazard for human spaceflight and is of particular concern for future manned missions to Mars, during which astronauts may be exposed to doses of approximately 1 Sv (*1*). Radiation in the space environment comes from trapped particle belts, solar particle events and cosmic rays (*2*). Protons (87%), helium ions (12%) and heavier ions (1%) compose the galactic cosmic ray (GCR) spectra. The health risks from exposure to these radiation types are difficult to quantify, notably because of limited knowledge of the biological effects of high-energy and high-charge (HZE) particles. In particular, HZE particles (fully or partially ionized ions from deep space) typically have a higher relative biological effectiveness (RBE) than low-linear energy transfer (LET) X rays and gamma rays for many biological end points, notably deoxyribonucleic acid (DNA) and chromosome damage (*3*).

Chromosomal aberrations (CAs) have been used in mechanistic studies of radiation effects, in biodosimetry and as possible biomarkers for carcinogenesis (*4*). The frequency of CAs in circulating lymphocytes is considered by many investigators to be a reliable indicator of biological dose. Indeed, it has been used to measure radiation exposures in nuclear accidents (*5*), in survivors of the Hiroshima and Nagasaki atomic bombings (*6*) and in

[1] Address for correspondence: NASA Lyndon B. Johnson Space Center, Mail Code SK, 2101 NASA Parkway, Houston, TX; e-mail: Ianik.Plante-1@nasa.gov.

Downloaded From: https://bioone.org/journals/Radiation-Research on 02 May 2024
Terms of Use: https://bioone.org/terms-of-use

astronauts exposed during spaceflight (*7*). Therefore, many experimental and theoretical studies have been conducted on radiation-induced CAs over the past few years, including mechanistic studies, biodosimetry, genomic instability and investigations of possible biomarkers for carcinogenesis (*8–14*), and more experiments are still ongoing. One of the difficulties in assessing chromosome damage experimentally is the need for an available technique that can provide a high-resolution assessment of all types of chromosome rearrangements simultaneously (*15*).

In this work, a new simulation program was developed and is presented here; the radiation-induced tracks, chromosome aberrations, repair and damage (RITCARD) program is used to simulate radiation-induced CAs in cells. This code is inspired by the program, NASA radiation track image (NASARTI) (*8, 9*). RITCARD was developed using modern software engineering practices to enable current and future model advancements (i.e., mixed-field and dose-rate simulations) to be implemented more efficiently and reliably. Although RITCARD and NASARTI are based on the same fundamental theoretical framework, the numerical implementation is different, with the new code, RITCARD, being more reliable, portable, efficient and well documented. NASARTI and RITCARD are both composed of four parts: a random walk (RW) algorithm for simulating chromosomes in a nucleus; radiation-induced DNA damage calculations; a break repair process; and a function to assess and count the types of CAs generated. RITCARD was used to calculate the yield of various types of CAs occurring in human fibroblast cells for many ions ($^{1}H^{+}$, $^{4}He^{2+}$, $^{12}C^{6+}$, $^{16}O^{8+}$, $^{20}Ne^{10+}$, $^{28}Si^{14+}$, $^{48}Ti^{22+}$ and $^{56}Fe^{26+}$) with energies varying from 10 to 1,000 MeV/n. The simulation results show linear and linear-quadratic dose dependence for most CA types, and the yields are relatively comparable to available experimental data. The coefficient of the linear part of the dose-dependence curve also peaks at a LET value of approximately 100 keV/μm, which evokes a RBE peak. Furthermore, the quadratic coefficient of the dose-response curve decreases with LET, suggesting that CAs caused by delta rays originating from several radiation tracks are more likely to occur at low LET. This program will be used to help analyze and understand results from CA experiments such as those performed recently at the NASA Space Radiation Laboratory, Brookhaven National Laboratories (NSRL).

MATERIALS AND METHODS

Code Programming and Maintenance

RITCARD is composed of several programs. The codes were made using the C++ programming language, version 98, using the Borland C++ environment. C++ classes are used extensively to model the various structures used in the program, such as chromosome fragments and reactive free ends. The classes are useful for modeling the objects, their attributes and their behaviors. The calculation part of the code is a console application that is platform-independent and also compiles and executes in Linux. It is also designed for execution in parallel on many central processing units (CPUs), both on a Linux cluster and on a Microsoft® Windows® (Redmond, WA) platform, as described elsewhere (*16*). In the Windows environment, a graphics user interface (GUI) is used to set up simulation parameters, whereas this is done manually in the Linux environment. Another GUI can be used to display the results in Windows. The tracks and the CAs can also be displayed with the RITRACKS OpenGL interface. That is, the Windows version is used mostly for development and testing of the code, whereas the Linux version is used for parallel execution of the code with large number of histories (production runs). The code is maintained and changes are tracked using the in-house GitLab environment accessible to NASA users, in compliance with NASA software engineering standards. A method toxicity metrics analysis was performed to assess the number of statements, the number of parameters, the depth of ''if'' functions and the cyclomatic complexity for each function of the code. For the calculation part, the maximum toxicity metrics score is 1.117, slightly exceeding the recommended threshold of 1.0. This score indicates that the code is well structured and in compliance with coding standards.

Part 1A: Simulation of chromosomes by random walk. The development of the chromosome simulation program that is a part of NASARTI spans several years (*17, 18*). Several updates have been made during this period, the most notable one in 2006 that included chromatin loops (*19*). Beginning in 2012, a CA simulation algorithm was implemented in NASARTI, but some coding errors were discovered during the course of this project and were resolved only recently. The RW model is based on the following principles:

1. The chromatin has physical and scaling properties analogous to those of long polymer chains;
2. A chromosome is roughly described by a random coil physical model;
3. Each chromosome is predominantly located in a part of the cell nucleus (domain);
4. Many large and intermediate-size DNA loops are present;
5. Telomeres are located at the extremities of the chromosomes, i.e., at the first and last ends of the RW.

Therefore, the simulation of chromosomes is done by a discrete RW, meaning that each chromosome is approximated by a coil comprising a series of monomers of 0.02 μm, each monomer containing 1 kbp of DNA. The nucleus can be modeled either as a sphere (e.g., for lymphocytes) or as an ellipsoid (e.g., for fibroblasts). In this work, since the simulations are done with fibroblast nuclei, the ellipsoid shape (height: 6 μm; large axis: 17 μm) is used. The extremities of the monomers occupy the points of a cubic lattice (X,Y,Z), where X, Y and Z are integers. The beginning of the chromosome (the first telomere) is determined by generating a position (X,Y,Z) randomly in the corresponding domain. The position of the next monomer is determined randomly and can be left (X-1,Y,Z), right (X+1,Y,Z), backwards (X,Y-1,Z), forward (X,Y+1,Z), down (X,Y,Z-1) and up (X,Y,Z+1). The process is repeated until the last monomer (the last telomere) is simulated.

The probability for each direction is equal at 1/6, but several constraints exist so that some directions may be forbidden during one step; therefore, these probabilities are different for some monomers. The new position of the monomer must be located inside the volume of the nucleus and in the domain of the chromosome. The option to use intermediate-size loops is also available. As described elsewhere (*19*), these loops are 60 monomeric units in length, separated by fragments of 60 monomer units. The program generates a subset of RW of 60 steps, until the last step of the RW returns to the original point of the loop.

The chromosome RW model included in the program NASARTI has been extensively validated, notably by pulse-field gel electrophoresis experiments (*17*). However, these calculations were made using large doses and amorphous track structures. For this work, since many new features have been added and stochastic track structures are used

Downloaded From: https://bioone.org/journals/Radiation-Research on 02 May 2024
Terms of Use: https://bioone.org/terms-of-use

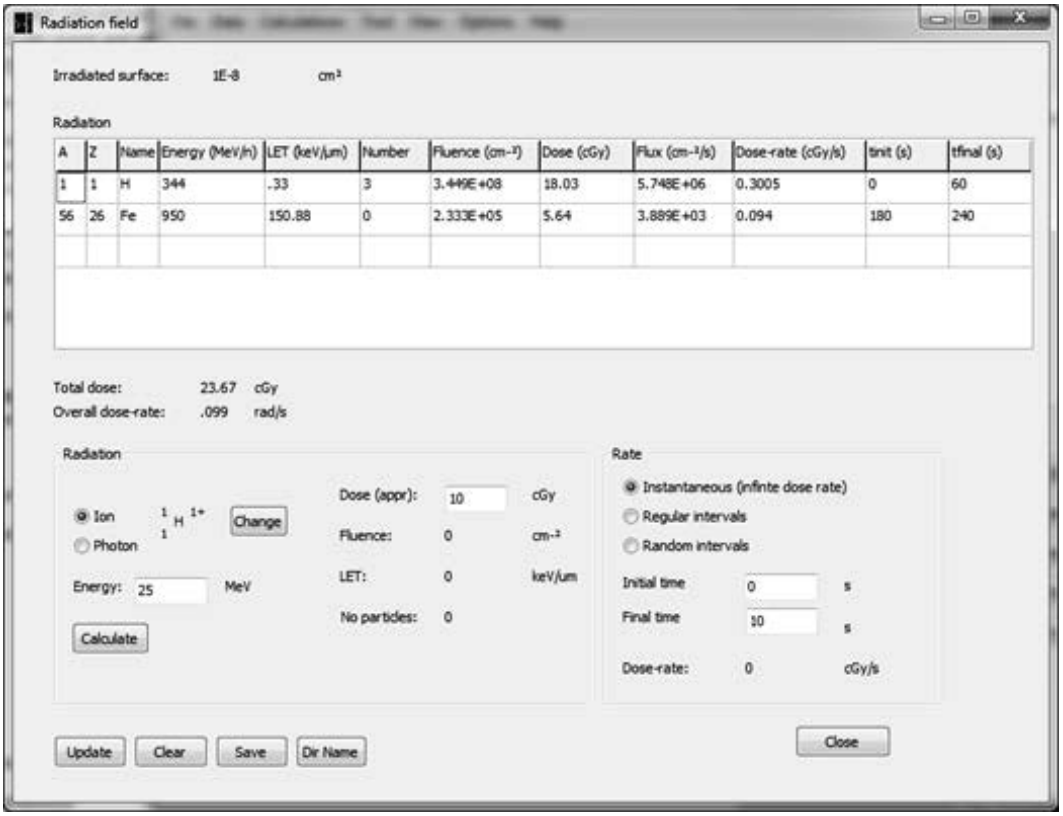

FIG. 1. Graphics user interface for entering multiple beam information in RITRACKS. For each contribution, the user must specify the ion type, the energy, the requested dose and the initial and final times of irradiation. Quantities such as the dose, the fluence, the flux, the LET and the dose rate are calculated by the program.

instead of amorphous tracks, the RW simulation routine was isolated from NASARTI, and is now a stand-alone program. Therefore, the RW simulation program pre-calculates nuclei that are used in RITCARD.

Part 1B: Simulation of volume irradiation by stochastic radiation tracks. Stochastic radiation tracks were simulated with the program RITRACKS, which has been described elsewhere (*20*). Briefly, RITRACKS calculates the energy deposition events, ionizations and excitations of water molecules by protons and HZE particles, as well as the energies, positions and directions of the secondary electrons and their full transport in an irradiated volume. The modeled cell nucleus was centered in a parallelepiped, which is considered the irradiated volume. Using calculated energy deposition, dose was calculated in voxels of 20 nm (*21*).

Previous versions of RITRACKS were used to simulate the irradiation of a parallelepiped or cylindrical volume with multiple tracks. However, the number of tracks was required to be fixed and identical for every simulation history. The type of ion and the energy were also required to be identical for each simulated ion. Additionally, all tracks are generated at time, $t = 0$. Recently, a new mixed-field functionality was added in RITRACKS. The new mixed-field functionality allows the simulation of the irradiation of a volume by multiple ion types and/or energies. The irradiation time should also be specified for each ion type and energy, which allows the program to simulate consecutive and/or overlapping beams.

For each simulation history, the number of tracks of each type impinging the volume is obtained by sampling from the Poisson distribution,

$$p(n) = \lambda^n e^{-n}/n!, \tag{1}$$

where $\lambda = \phi A$ is the average number of tracks, ϕ is the fluence and A is the area of the irradiated surface. The value of ϕ is obtained from a given dose using the well-known equation:

$$D(Gy) = 1.6 \times 10^{-9} \phi\left(cm^{-2}\right) LET(keV/\mu m) \tag{2}$$

The LET of a particle is calculated using the Bethe equation (*22*).

The user also needs to specify the time interval for each particle type. It is therefore possible to simulate consecutive or overlapping beams using the code. The GUI to enter mixed fields data is shown in Fig. 1.

The grid shows the summary of each ion type and energy. The contribution of each beam type can be modified. In principle, there are no limits on the number of particle types and energies to use in the simulation. For this work, the calculations are limited to one ion type of one energy, with acute dose rate (i.e., all tracks are simulated at time, $t = 0$).

Calculations performed using RITRACKS led to the discovery that the dose calculated in the nucleus was significantly lower than the requested dose, by up to 25%, especially for ions with high energy per nucleon. An investigation of this problem revealed that a significant amount of the energy is not deposited in the irradiated volume due to secondary electrons escaping. To improve the calculated dose, we first attempted to increase the size of the irradiated area. However, for particles of moderate to high energies, many secondary electrons have sufficient energy to leave the irradiated volume. For instance, electrons with energy in the MeV range can travel up to 100 mm (*23*); thus, increasing the size of the irradiated area did not help much. In actual experiments, we would also expect secondary electrons from neighboring volumes to contribute to energy deposition in the volume under consideration. To consider this, we simulated the contributions

Downloaded From: https://bioone.org/journals/Radiation-Research on 02 May 2024
Terms of Use: https://bioone.org/terms-of-use

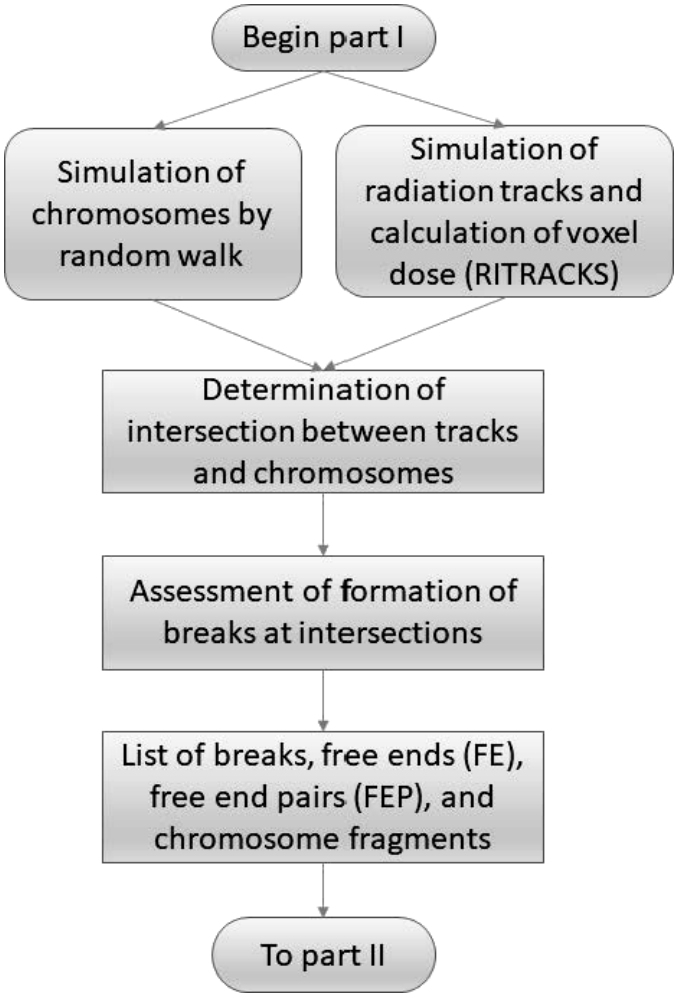

FIG. 2. Schema showing the first part of the program, leading to the formation of breaks, free ends, free end pairs and chromosome fragments.

from the electrons originating from outside the irradiated volume by using periodic boundary conditions (PBC). We have found that using PBC significantly improves the dose calculations, with values very close to the predicted values given by using the Bethe equation. However, PBC is an imperfect approach. For example, at low doses the electron tracks that return to the irradiated volume after crossing a boundary represent secondary electron tracks generated by ion tracks impinging neighboring volumes. At low doses these tracks occur at a time that is different from the ion track actually impinging the irradiated volume. For this work, since acute dose rates were used for the simulation, this is not expected to influence the results.

Part 1C: Simulation of chromosome breaks. Previously, NASARTI was used to calculate the number and distribution of double-strand breaks (DSBs) within nuclei, using amorphous track calculations of the radial dose combined with chromosome models simulated by random walk (*8, 9*). In this code, which is used essentially for comparison in this work, the probability (Ψ) to find at least one DSB at a monomer located in a voxel is given by Eq. (3),

$$\Psi = 1 - e^{-QD(i,j,k)}, \tag{3}$$

where $D(i,j,k)$ is the local (voxel) dose, i, j and k are the spatial coordinates of the voxel (in lattice units), and Q is an adjustable parameter representative of the intensity of the stochastic process of DSB formation. In this work, $Q = 1.14 \times 10^{-5}$ Gy^{-1}. Since several tracks (*ntracks*) may be present, $D(i,j,k)$ is calculated as

$$D(i,j,k) = \sum_{l=1}^{ntracks} D(r_l), \tag{4}$$

where r_l is the radial distance to track l. In RITCARD, the simulation of chromosome breaks is done the same way, but stochastic tracks are used instead of amorphous tracks. Equation (3) is also used for calculating the breaks at specific monomers of the chromosomes. However, since stochastic tracks are used, the voxel dose values are obtained from the three-dimensional (3D) voxel dose map (*21*). To include possible dose-rate effects, the creation time of the break is also obtained by using the corresponding time in the voxel. A schema summarizing the first part of the program is shown in Fig. 2.

Part 2: Repair of breaks. In Part 1, the program calculates the break locations in the chromosomes. Similar to a rope, each break results in the formation of two fragments. An example of fragments generated by the program is shown in Fig. 3.

The newly created extremities are reactive free ends. The free end pairs are organized into a list, and each reactive free end pair can be repaired. The repair of reactive free ends that originates from the same break (e.g., the free ends no. 2 and 3 in Fig. 3) is a proper rejoining; otherwise, it is an improper repair. The relevant files generated by the program are described in detail in Appendix 1.

```
Fragments

Tel                     0 1                       2 3                       4 5                     Tel
o>>>>>>>>>>C> 0>>>>>>>>>>>>x x>>>>>>>>>>>> 0>>>>>>>>>>>>x x>>>>>>>>>>>> 0>>>>>>>>>>>>x x>>>>>>>>>>>> 0>>>>>>>>>>>>o

Tel                     6 7                     Tel
o>>>>>>>>>>>>18>>>>>>>>>>>>x x>>>>>>>>>>>C>18>>>>>>>>>>>>o

Tel                     8 9                      10 11                    Tel
o>>>>>>>>>>>C>23>>>>>>>>>>>>x x>>>>>>>>>>>>23>>>>>>>>>>>>x x>>>>>>>>>>>>23>>>>>>>>>>>>o

Tel                    12 13                    Tel
o>>>>>>>>>>>>24>>>>>>>>>>>>x x>>>>>>>>>>>C>24>>>>>>>>>>>>o

Tel                    14 15                    Tel
o>>>>>>>>>>>C>28>>>>>>>>>>>>x x>>>>>>>>>>>>28>>>>>>>>>>>>o
```

FIG. 3. Fragments. The numbers on the first line indicate the index of the reactive free end, or if it is a telomere (Tel). In the second line, ''o'' is a telomere, ''x'' is a free end, ''C'' indicates a centromere and ''>'' represents the direction of the DNA (3′–5′). The numbers in the second line indicate the chromosome number (1–45). Chromosome 0 has three breaks, resulting in four fragments. Chromosomes 18, 24 and 28 have two breaks, resulting in two fragments each. Chromosome 23 has two breaks, resulting in three fragments. The various counts in this file and others generated by RITCARD start at 0, since the first elements of arrays and vectors in C++ are indexed as 0.

Downloaded From: https://bioone.org/journals/Radiation-Research on 02 May 2024
Terms of Use: https://bioone.org/terms-of-use

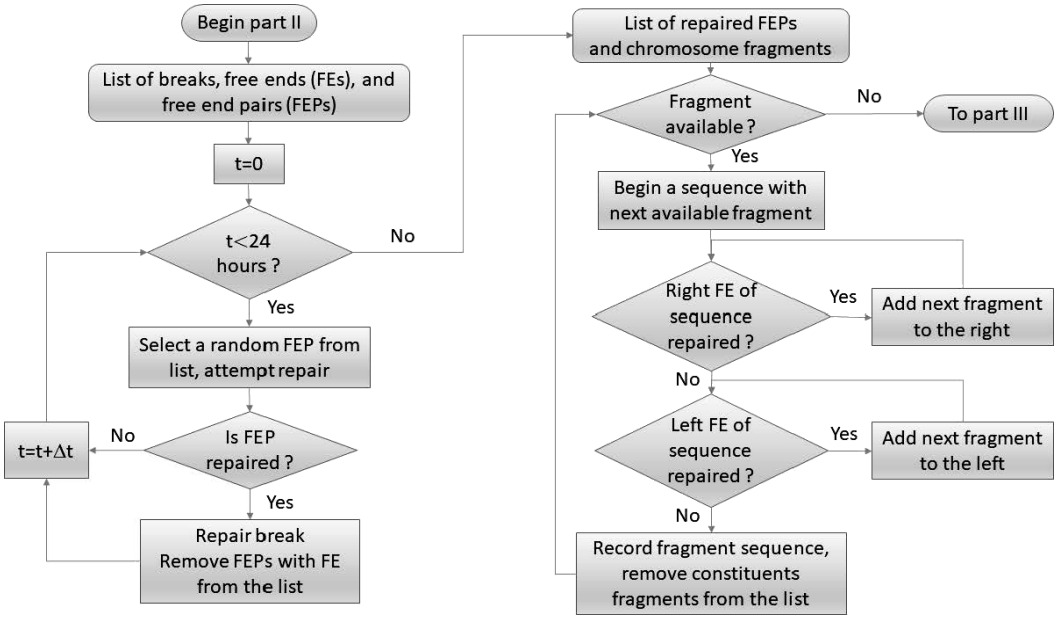

FIG. 4. Repair algorithm in RITCARD, illustrating the repair of broken chromosomes (left part) and the formation of fragment sequences (right part).

In this part of the program, the breaks are repaired using an algorithm that follows the structure of NASARTI. The program uses time steps of 5.18 s, for 24 h. The value of this time step was obtained from prior calibration of the model, in which the DSB repair kinetics are fitted as a bimodal exponential curve (*9*). At each time step, the program picks a free end pair randomly. If the free ends originate from the same break, it is a proper rejoining, which is repaired with probability $P = 1$. Otherwise, it is an improper repair. In this case, the probability of repair depends on the 3D Euclidian distance between broken ends as in Eq. (5),

$$I = \frac{1}{W} e^{-r^2/\sigma^2}, \tag{5}$$

where I, is the probability of an improper rejoining (misrejoining) in an elementary step of the algorithm; W is an empirically calibrated parameter; r is a 3D Euclidian distance between reacting DSB free end (μm); and σ is an adjustable parameter with the dimension of microns. Another condition that needs to be fulfilled for a break to repair is that the break must have been already created at the time of repair. This condition is added to consider possible dose-rate effects. When a free end pair is repaired, all free end pairs containing these free ends are removed from the list of free end pairs, so they do not participate in the repair process any further.

After the repair algorithm is complete, RITCARD analyzes the repaired chromosomes. At this point, RITCARD diverges from NASARTI; that is, it is using a different, but equivalent, algorithm. Briefly, the program is building new objects, named fragment sequences, which are composed by chromosome fragments. A new sequence begins with the first fragment comprising a free end. Then, if a free end is present on the right side, the program inspects the list of repaired free ends to find if it has been repaired. If it is the case, the fragment to which the other free end of the pair belongs is added to the right of the sequence. If the last free end of the fragment is selected, the added fragment is in reverse order. The other end of the fragment is then examined. If it is a telomere, the repair process is over from this side; otherwise, the process is repeated until the last free end is a telomere or not repaired. The repair process is complete on the right side. If the initial fragment does not begin with a telomere, the repair process is repeated from the left side. The repair algorithm is illustrated in Fig. 4.

Part 3: Classification of chromosome aberrations. During the repair process, the fragments are rejoined, which leads to the formation of fragment sequences. Figure 5 illustrates one possibility of fragment sequences for the fragments shown in Fig. 3 (a more detailed file is shown in the Appendix).

The fragment sequences generated are not only a clear visualization of the formation of CAs but also highly useful for verifying that they are correctly identified by the algorithm.

A detailed review of CA types is given in (*24*). The code detects intact chromosomes (properly repaired), terminal deletions, deletions, inversions, intrachromosomal translocations, simple exchanges, rings, dicentrics, open fragments and complex aberrations. These aberration classes are not necessarily exclusive; for example, a ring can also be a dicentric.

To determine the CA types it is convenient to group sequences containing material originating from the same chromosomes. The groups for the case illustrated in Fig. 5 are listed in Table 1.

```
Group number: 1
--------------------------------------------------

Tel                        6 9                        10 11                      Tel
o>>>>>>>>>>>>18>>>>>>>>>>>>x x>>>>>>>>>>>>23>>>>>>>>>>>>x x>>>>>>>>>>>>23>>>>>>>>>>>>o  1       1       62925          Exchange P1

Tel                        8 7                       Tel
o>>>>>>>>>>C>23>>>>>>>>>>>>x x>>>>>>>>>>C>18>>>>>>>>>>>>o       1       1       80575          Polycentric     Exchange P2
```

FIG. 5. Fragment sequences. As in Fig. 3, the numbers on the first line of each sequence indicate the index of the free end, or if it is a telomere (Tel) ''o'' is a telomere, ''x'' is a free end, ''C'' indicates a centromere and ''>'' represents the direction of the DNA (3–5′). The numbers in the second line indicate the chromosome number.

Downloaded From: https://bioone.org/journals/Radiation-Research on 02 May 2024
Terms of Use: https://bioone.org/terms-of-use

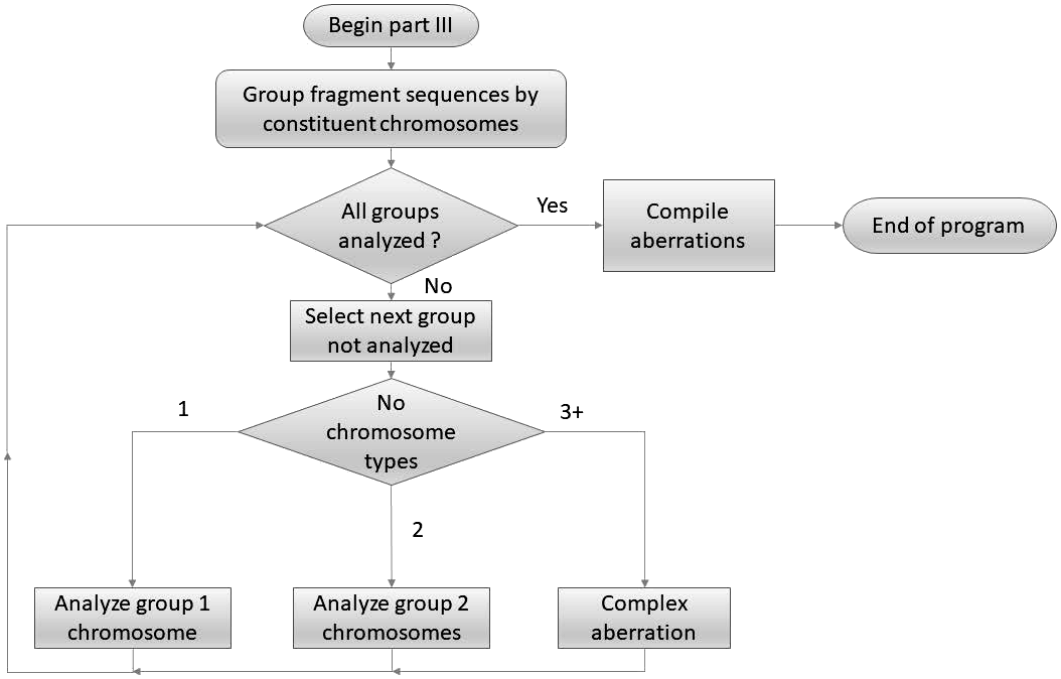

FIG. 6. Schema showing an overview of the analysis of the groups of chromosome fragments. As mentioned in the text, the program analyzes the fragment sequences group by group.

The classification algorithms (Figs. 6–8) consider each group of fragment sequences separately. In the beginning of this part, the program determines the number of chromosomes present in the group and analyzes the sequences accordingly. The groups containing fragments with material from one chromosome are analyzed, as shown in Fig. 7. Similarly, groups containing fragments with material from two chromosomes are analyzed, as shown in Fig. 8. The groups containing fragments from three or more chromosomes are necessarily complex aberrations.

Cell Culture

hTERT-immortalized normal human skin fibroblast cells 82-6 (*25*), kindly provided by J. Campisi (Lawrence Berkeley National Laboratory, Berkeley, CA), were grown as monolayers at 37°C under 5% CO_2 in DMEM (Gibco®/Invitrogen™, Carlsbad, CA) supplemented with 10% fetal bovine serum, antibiotic-antimycotic (1×) and L-glutamine (2 m*M*). Cells were irradiated in confluent state with accelerated ions, as described in the next section.

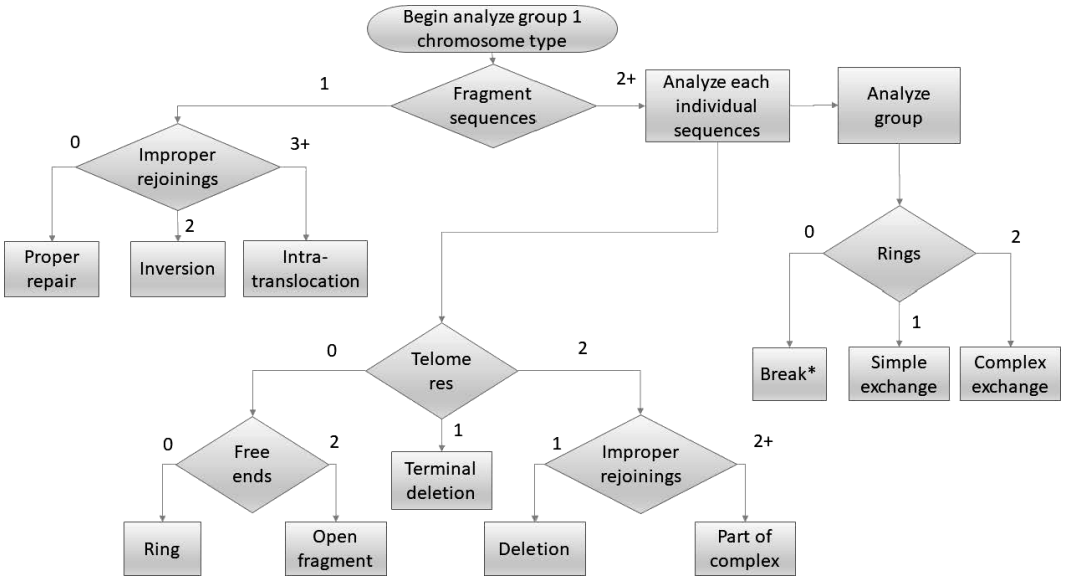

FIG. 7. Classification of aberration types in groups containing fragments from one chromosome. In the schema, a break is a type of aberration not considered in the program for now.

Downloaded From: https://bioone.org/journals/Radiation-Research on 02 May 2024
Terms of Use: https://bioone.org/terms-of-use

TABLE 1
Group Sequences with Material from the Same Chromosomes (Fig. 5)

Group number	Chromosome type(s)[a]	Sequence number(s)
0	{0 }	{0 }
1	{18 23 }	{1 2 }
2	{24 }	{3 }
3	{28 }	{4 }

[a] Chromosome types contained in the sequence.

Irradiation

Cells were grown in T25 flasks, and irradiated with proton (250 MeV), helium (250 MeV/n), oxygen (350 MeV/n) and titanium (300 MeV/n) ions at NSRL. Dose rates were between 0.5 and 40 cGy/min, depending on the dose delivered. Flasks were filled with media during irradiations.

Premature Chromosome Condensation (PCC)

The PCC technique was used to collect G_2/M-phase chromosomes as previously described elsewhere (*12, 13, 26*). After irradiation, fibroblast cells were allowed to repair for 16 h, and then subcultured at low-cell-population density. After 10-h incubation, cells were arrested in mitosis by adding colcemid to a final concentration of 0.1 μg/ml in the culture media, then cells were incubated for an additional 6 h. Approximately 30 min before collection, 50 n*M* of calyculin A (Wako Pure Chemical Industries Ltd., Osaka, Japan) was added to the culture media to condense the chromosomes in the G_2 phase of the cell cycle.

Fluorescence In Situ Hybridization (FISH)

Chromosomes were hybridized *in situ* with a combination of three fluorescence whole chromosome human DNA probes for chromosomes 1 (red), 2 (green) and 4 (yellow) (Aquarius®, Cytocell, Oxford Gene Technology, Oxfordshire, UK), using the protocol recommended by the manufacturer. Background chromosomes were stained with 4′,6-diamidino-2-phenylindole (DAPI). Chromosomes were analyzed with Leica CytoVision® FISH system that includes Leica fluorescent microscope with charge-coupled device (CCD) camera and karyotyping software (Nussloch, Germany). The images of all damaged cells were captured electronically. Complex exchanges were scored when it was determined that an exchange involved a minimum of three breaks in two or more chromosomes (*27*). An exchange was defined as simple if it appeared to involve two breaks in two chromosomes, that is, dicentrics and translocations. Incomplete translocations and incomplete dicentrics were included in the category of simple exchanges, assuming that in most cases the reciprocal fragments were below the level of detection. Each type of exchange (dicentrics, apparently simple reciprocal exchanges, incompletes or complex) was counted as one exchange, and values for total exchanges were derived by adding the yields. When two or more painted chromosomes were damaged, each was scored separately. For each experiment consisting of a single beam at multiple doses, at least 1,000 cells were scored for each data point.

Statistical Analysis

The frequencies of CAs in the painted chromosome(s) were evaluated as the ratio between aberrations scored and total cells analyzed, and extrapolated to whole genome equivalent using a modified version of the Lucas *et al.* formula (*14, 28, 29*). Standard errors for aberration frequencies were calculated assuming Poisson statistics. Error bars in each figure represent standard errors of the mean values. The area of the cell nucleus of the 82-6 cells was determined by confocal microscopy with fixed cells at 162.0 μm^2.

Background Subtraction

For comparison of experimental data with modeling results, the background level of CAs present in the cells needed to be subtracted from the results measured for irradiated cells. Consistent with the usual assumption of Poisson statistics, this subtraction was performed by direct Monte Carlo sampling. The average number of CAs from nonirradiated control cells and irradiated cells were obtained in the experiment and assumed to follow Poisson distributions. These distributions were sampled numerically using Monte Carlo methods in an uncorrelated manner, and subtraction was performed on a trial-by-trial basis (i.e., number of CAs sampled from background distribution was subtracted from number of CAs sampled from irradiated distribution). This process formed a new distribution representing the radiation-induced CAs in irradiated cells from which a mean and standard error could be computed. In general, the means obtained from this process were nearly identical to what would be obtained if the average measured values were subtracted directly. The errors were similar to what would be obtained if the measured errors were combined in quadrature. However, this process also allowed us to identify background-subtracted experimental values that were statistically greater than zero (i.e., irradiated cells with CA levels significantly above background levels) at a 95% confidence level. These experimental values are noted on the plots presented later in this article.

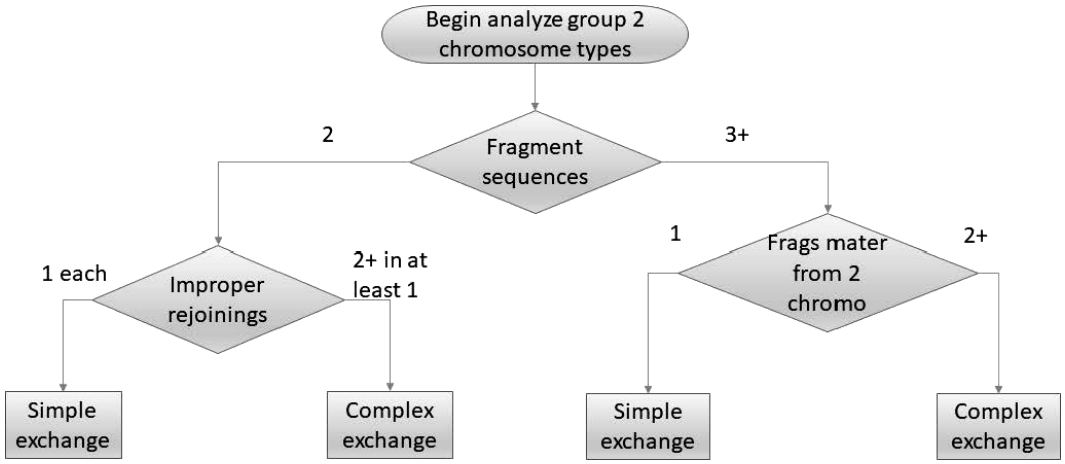

FIG. 8. Classification of aberration types in groups containing fragments from two chromosomes.

Downloaded From: https://bioone.org/journals/Radiation-Research on 02 May 2024
Terms of Use: https://bioone.org/terms-of-use

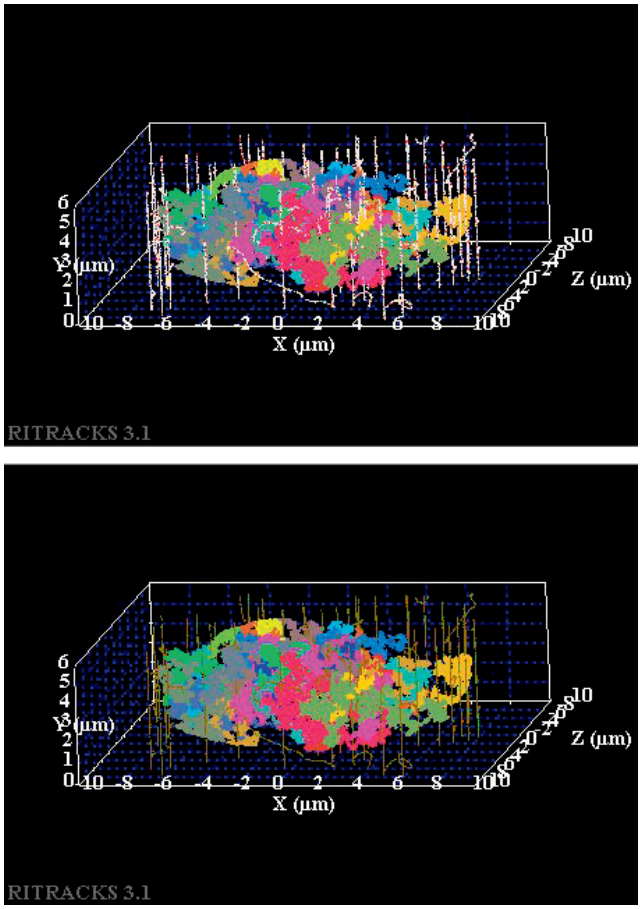

FIG. 9. Simulation of the irradiation of a fibroblast nucleus by 10-MeV protons, at a dose of 10 cGy. The tracks are shown on the top panel, with each dot representing a radiolytic species created, and the corresponding dose voxels (20 nm in size) are shown on the bottom panel.

RESULTS AND DISCUSSION

Simulation of Radiation Tracks and Nuclei

The first part of the program is the calculation of nuclei chromosomes by RW and stochastic tracks. An example of a fibroblast nucleus irradiated by proton tracks is given in Fig. 9. The nucleus is an ellipsoid of dimensions 17 µm × 17 µm × 6 µm. The chromosomes are different colors, occupying clearly visible domains. The tracks and voxels are confined to the irradiation box encompassing the nucleus, due to periodic boundary conditions.

Fragment Size Distribution

Simulation of chromosome breaks results in the formation of fragments of different length. The distributions of fragment sizes were obtained using RITCARD and NASARTI for a simulation of $^{16}O^{8+}$, 350 MeV/n, with a dose of 0.4 Gy and 100,000 histories. The bin size is 1 monomer. Results are shown in Fig. 10.

The vertical lines observed at over 10,000 monomer units correspond to intact chromosomes. The smaller fragments are generated by the chromosome breaks. The fragment size distributions obtained from NASARTI and RITCARD are essentially indistinguishable; therefore, these two codes yield mostly equivalent results at this stage of the simulation.

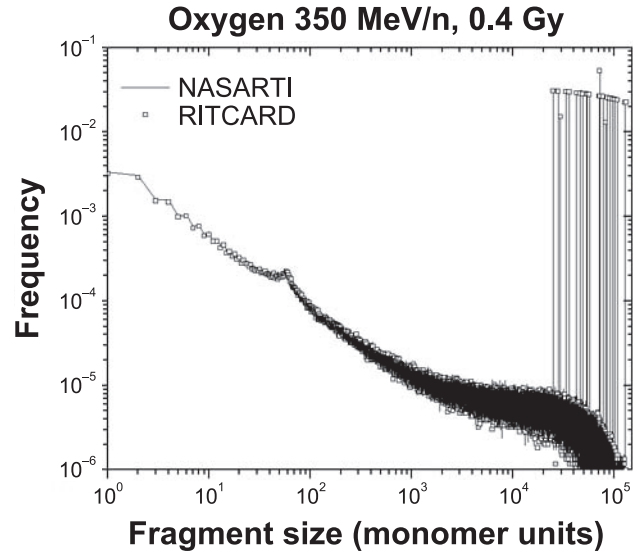

FIG. 10. Fragment size distribution for a nucleus irradiated by $^{16}O^{8+}$, 350 MeV/n, at a dose of 0.4 Gy, as calculated by the programs RITCARD (symbols) and NASARTI (line).

Repair Kinetics

Repair kinetics curves are obtained by recording the time at which breaks are repaired, and averaging over all simulation histories (Fig. 11). The proper and improper rejoined breaks are recorded separately.

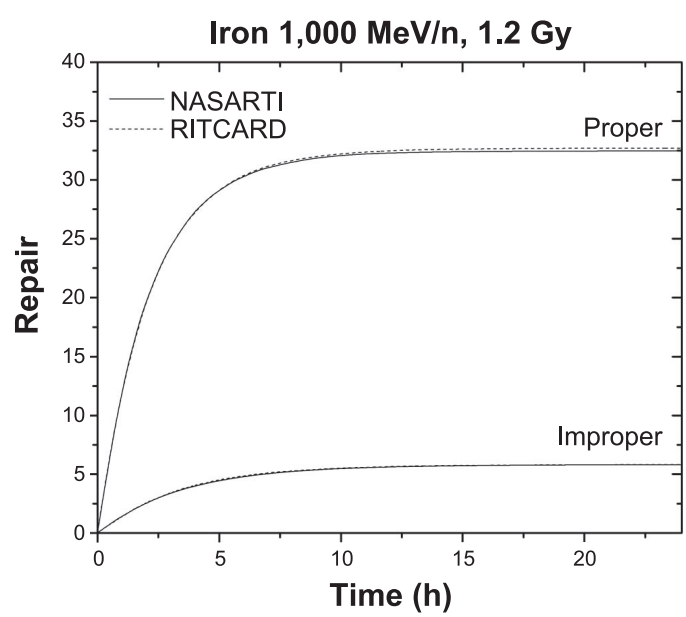

FIG. 11. Repair kinetics curves for a 1-GeV/n iron ion, 1.2 Gy. The calculations by NASARTI and RITCARD are almost identical.

Downloaded From: https://bioone.org/journals/Radiation-Research on 02 May 2024
Terms of Use: https://bioone.org/terms-of-use

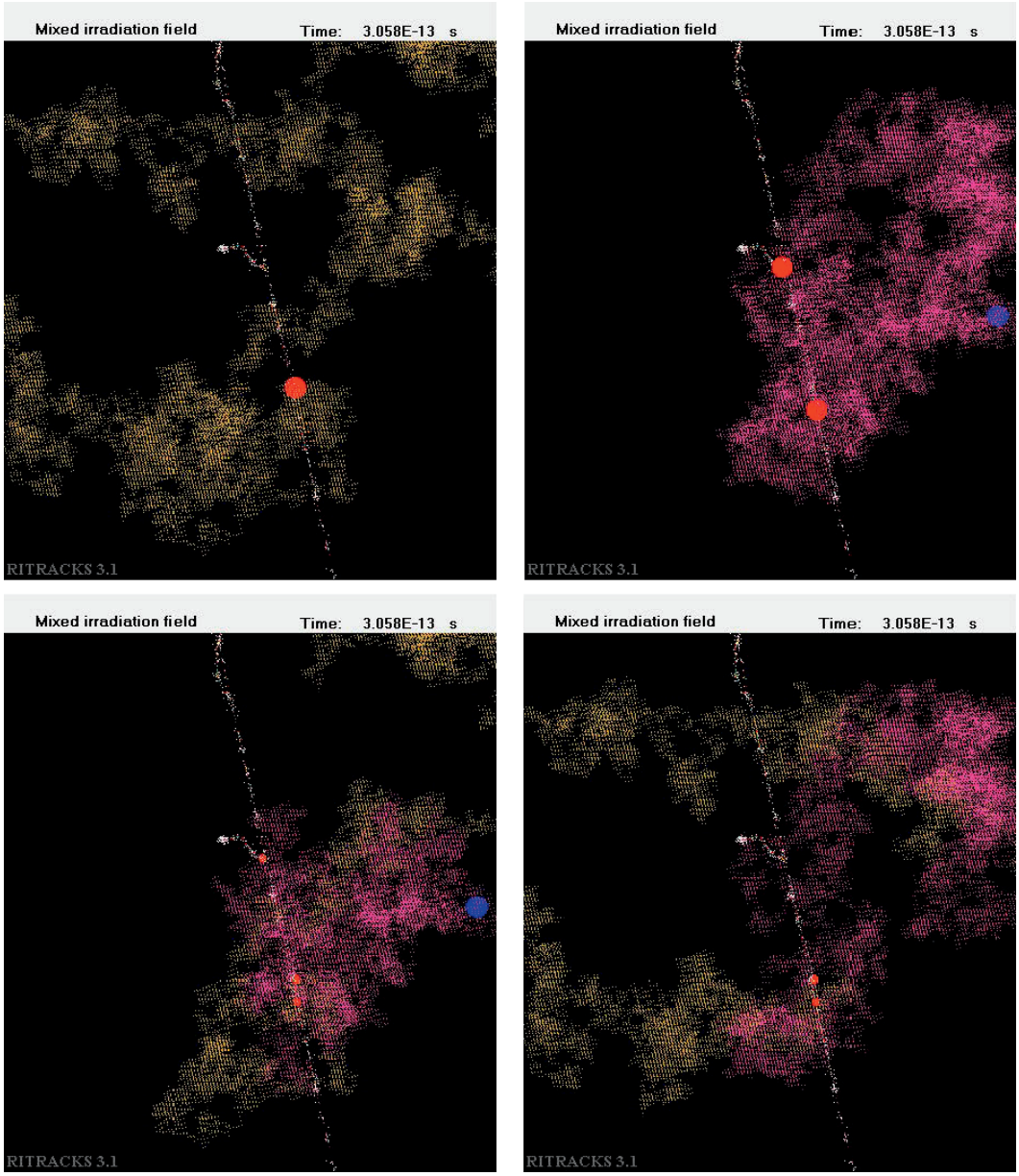

FIG. 12. Illustration of a radiation-induced simple exchange between chromosomes 18 and 23. The nucleus is irradiated by protons, 0.1 Gy. For clarity, only one track is shown. Panels A and B: The intact chromosomes 18 and 23 are shown, with a telomere shown in blue. They are both intersected by a radiation track, which damages the chromosomes (shown in red). Chromosome 18 has one break, whereas chromosome 23 has two. Panels C and D: The fragments are misrejoined, which leads to an exchange.

We have performed several tests on the restitution kinetics. As discussed elsewhere (*9*), the number of remaining breaks as a function of time is often approximated by a bi-exponential decay curve. We have observed that in general, the CA yields are not very sensitive to the shape of the restitution kinetics curve, and that parameters such as the decay times do not influence the results by much. The reason is that the repair is largely dominated by proper repair, which does not lead to aberrations. As the irradiation is delivered at time, $t = 0$, for this work, most breaks are repaired at 24 h. The most important thing that influences the CA yields appears to be the ratio between the proper and improper repair at 24 h.

Chromosome Aberrations

The RITRACKS OpenGL interface allows for visualization of CAs, as shown in Fig. 12. The visualization interface clearly illustrates the interaction of tracks leading to a CA, which is a powerful verification and validation tool for the program.

It is also possible to visualize other types of aberrations. However, in many cases, especially for high-LET radiation,

Downloaded From: https://bioone.org/journals/Radiation-Research on 02 May 2024
Terms of Use: https://bioone.org/terms-of-use

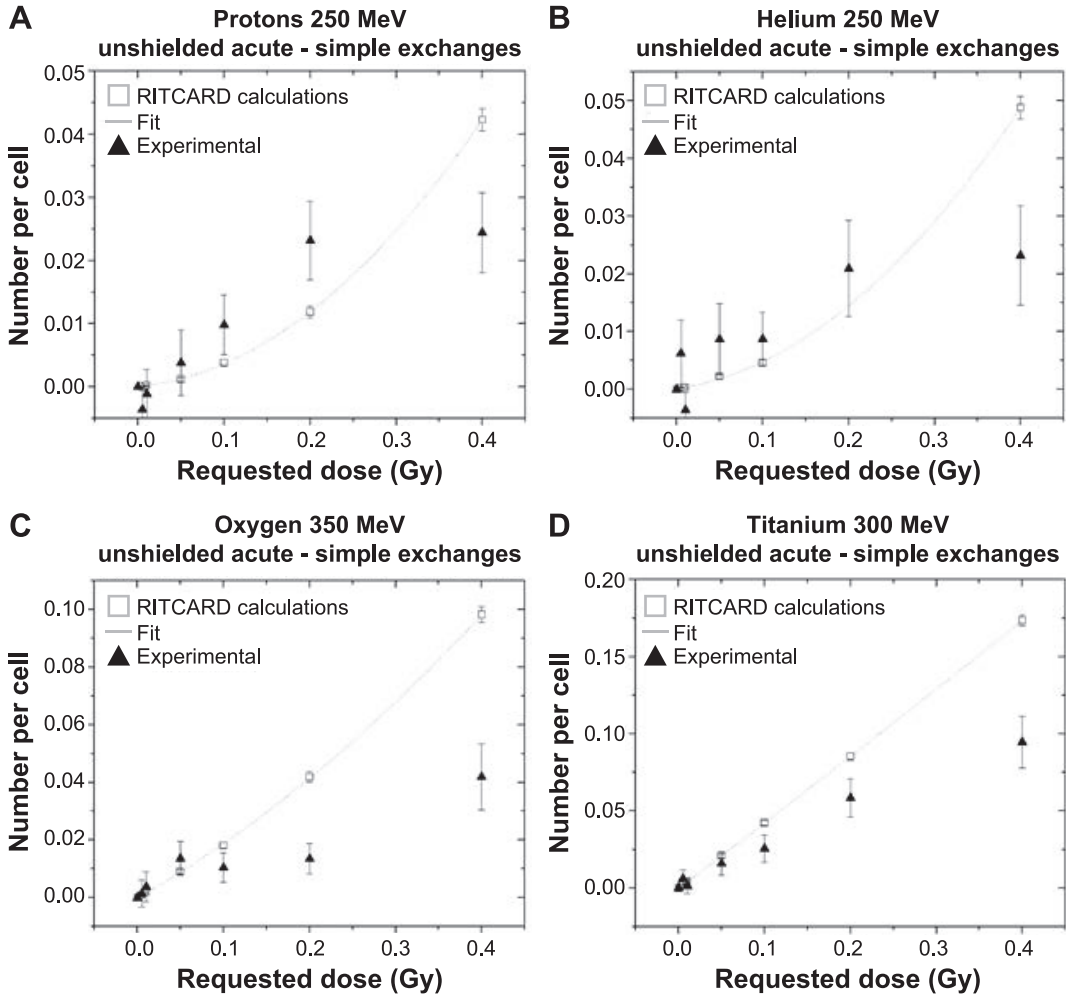

FIG. 13. Dose-response curves for simple exchanges for (panels A–D) 250 MeV protons, 250 MeV/n helium, 350 MeV/n oxygen and 300 MeV/n titanium, respectively.

many breaks occur in close proximity and the fragments are rather small. For example, as shown in Fig. 5, we observe that most fragments created by the breaks are smaller than 10 monomer units. Since most aberrations involve small fragments, they are difficult to see even under magnification.

The program RITCARD was used to calculate the yield of various types of CAs for a number of ions ($^{1}H^{+}$, $^{4}He^{2+}$, $^{12}C^{6+}$, $^{16}O^{8+}$, $^{20}Ne^{10+}$, $^{28}Si^{14+}$, $^{48}Ti^{22+}$ and $^{56}Fe^{26+}$), with energies varying from 10 to 1,000 MeV/u. The error on the results was estimated using 1.96 times the standard error on the mean, so that they should represent a confidence interval of 95%. Each data point was calculated using 100,000 simulation histories. Selected dose-response curves are shown in Fig. 13. The corresponding experimental data are included in Table 2. In Fig. 13, we observe that the simulation results can be well approximated by a linear-quadratic curve:

$$CA = \alpha D + \beta D^2 \tag{6}$$

In general, experimental results are in good agreement with the simulation results at low dose. At higher dose, the experimental results are lower than the simulation results. Furthermore, it is difficult to infer any conclusion on a trend, notably due to large error bars and lack of points at higher doses. At this time, the cause of this discrepancy is not clear. In the repair process implemented in the code, the rejoining probability is exclusively function of the Euclidian distance, and no restrictions are imposed on the fragment length. It is possible that experiments are unable to detect CAs containing very small fragments, or that allowing CAs to occur with fragments of any length in the simulation model overestimates the number of CAs.

Notably, experimental techniques usually cannot detect all aberrations at once. For example, in the FISH technique, probes are used to paint chromosomes 1 in red, 2 in green and 4 in yellow. All other chromosomes are stained with DAPI. Using this technique, a subset of the exchanges in the sample can be detected, so that the number counted by the experimentalist must be multiplied by a factor to extrapolate the number of exchanges occurring in the entire genome.

Downloaded From: https://bioone.org/journals/Radiation-Research on 02 May 2024
Terms of Use: https://bioone.org/terms-of-use

TABLE 2
Experimental Data

Ion	Energy (MeV/n)	Dose (cGy)	Cells scored	Simple exchanges per cell	Error	Background subtracted	Error
-	-	0	4,908	0.0061	0.0017	0	0
Proton	250	0.5	1,002	0.0025	0.0025	–0.0035856	0.00302853
		1	1,005	0.0049	0.0035	–0.0011273	0.00390138
		5	1,006	0.0049	0.0049	0.0037942	0.00522816
		10	2,031	0.0159	0.0044	0.0098025*	0.0047344
		20	2,034	0.0292	0.006	0.0231803	0.006221
		40	2,032	0.0305	0.0061	0.0244285*	0.0063436
Helium	250	0.5	1,007	0.0123	0.0055	0.0062452	0.00577277
		1	1,002	0.0025	0.0025	–0.0035856	0.00303019
		5	1,011	0.0147	0.006	0.00864756	0.00625124
		10	2,015	0.0148	0.0043	0.0086986*	0.004609
		20	1,011	0.027	0.0081	0.0209027*	0.0083128
		40	1,016	0.0293	0.0084	0.023209*	0.0086298
Oxygen	350	0.5	1,004	0.0074	0.0043	0.0013457	0.00461948
		1	1,005	0.0099	0.0049	0.00380401	0.00523206
		5	1,512	0.0197	0.0057	0.013608*	0.0059423
		10	1,807	0.0165	0.0048	0.0103973*	0.0050657
		20	2,025	0.0196	0.0049	0.0135206*	0.0051979
		40	930	0.48	0.0113	0.0419026*	0.0114402
Titanium	300	0.5	1,007	0.0123	0.0055	0.00624519	0.0057728
		1	1,004	0.0074	0.0043	0.00134571	0.0046177
		5	1,009	0.0221	0.0074	0.0160444*	0.0075725
		10	1,016	0.0317	0.0088	0.025648*	0.008964
		20	1,036	0.0646	0.0124	0.0585224*	0.0125527
		40	911	0.1006	0.0165	0.0945846*	0.01664

* The lower 95% confidence limit is above 0.

Calculation of α and β coefficients

The dose-response curves for all ions simulated were fitted by a linear-quadratic curve [Eq. (6)] in Origin software using the built-in functions. The coefficients α and β and the standard errors on their values were calculated. The coefficients α and β of the fitted curves are shown in Fig. 14. The program clearly shows that there is a peak in the α component at approximately 100 keV/μm. This is an important finding, since such a peak is observed for many measurable end points, including in chromosome aberration simulations (*11*) and experiments (*7, 29, 30*).

TABLE 3
Values of α and β Calculated from Fitting of the Simulation Results

Ion	Energy (MeV/n)	LET (keV/μm)	α	Error	β	Error
Proton	1,000	0.22	0.00927	0.00297	0.22276	0.0029
Proton	250	0.39	0.01314	1.72E–04	0.23118	0.00397
Proton	10	4.59	0.05314	0.01272	0.21661	0.01246
Helium	250	1.56	0.02208	0.00444	0.24893	0.01065
Helium	100	2.91	0.05306	0.00757	0.26664	0.00741
Helium	13	14.83	0.17261	0.00943	0.18492	0.00924
Carbon	25	78	0.44999	0.03013	0.06843	0.02951
Carbon	600	9.18	0.09095	0.01062	0.20558	0.0104
Carbon	10	163.77	0.50082	0.00465	–0.01862	0.00456
Oxygen	350	20.7	0.16886	0.00408	0.19213	0.01014
Oxygen	128	38.89	0.26554	0.00706	0.18367	0.00692
Oxygen	77	56.75	0.35628	0.02185	0.17165	0.02139
Neon	267	37.54	0.28568	0.0222	0.14811	0.04156
Neon	64	102.33	0.50709	0.02517	0.0374	0.02465
Silicon	93	150.53	0.54407	0.04741	–0.02695	0.04643
Titanium	300	170	0.42171	9.30E–04	0.03061	0.00231
Titanium	240	193.58	0.42081	0.02364	0.02692	0.02579
Iron	600	172	0.41571	0.00211	0.04736	0.01163
Iron	130	405	0.27522	0.02752	0.0335	0.02666
Iron	60	716	0.2267	0.01264	–0.00864	0.01238
Photons	0.6617	0.8	0.04207	0.015	0.20967	0.01502

Downloaded From: https://bioone.org/journals/Radiation-Research on 02 May 2024
Terms of Use: https://bioone.org/terms-of-use

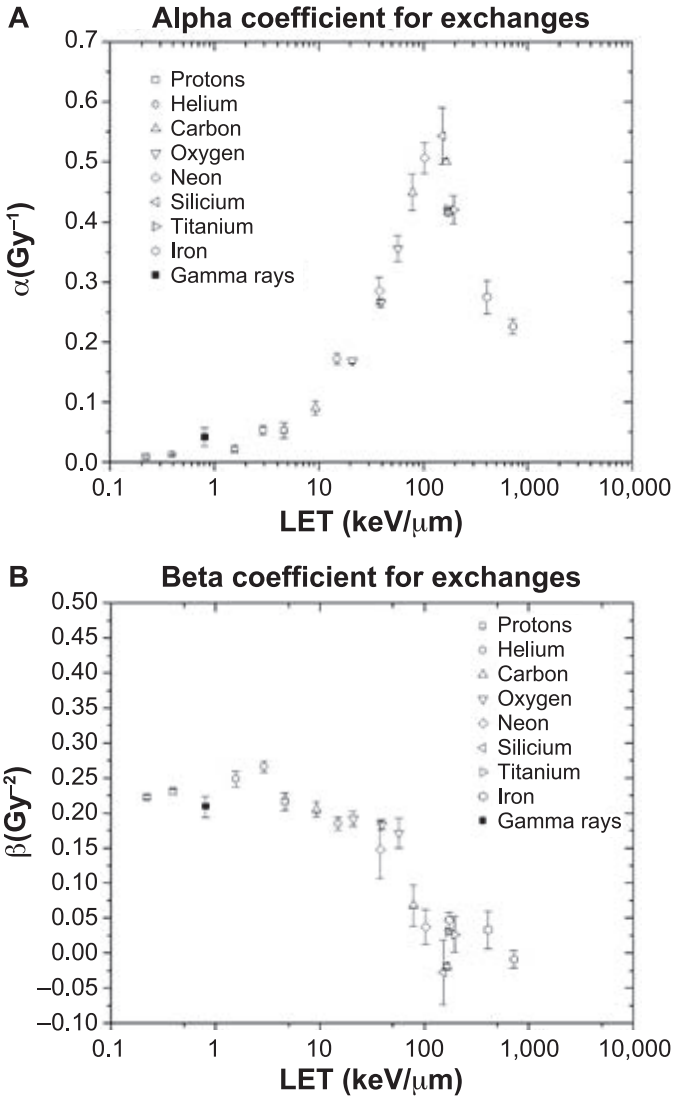

FIG. 14. Coefficients alpha (panel A) and beta (panel B) of the dose response curves, as a function of LET, for chromosome exchanges, as calculated by RITCARD.

Notably, this peak appears naturally from the calculations without doing specific assumptions in the model.

The results in Fig. 14 (right) show that the quadratic component appears to be less important for high-LET ions. This trend is in line with the analysis made by Loucas *et al.* (*14*), as they used purely linear models for high-LET ions. As reported by Loucas *et al.* (*14*), for photon irradiation the linear portion is thought to be the consequence of the misrejoining of break pairs formed by ionizations that occur along a single electron track that is set in motion by photo-absorptive events. These events dominate at low doses and low dose rates and are independent of dose rate. At higher doses and dose rates, contribution from the β coefficient begins to dominate and the interaction of breaks caused by independent electron tracks becomes more likely. This process also leads to misrejoining involving two or more breaks, and results in a dose-dependent curvature in the dose response, which is profoundly affected by dose rate. In stark contrast, low-energy charged particles, such as those from naturally emitted alpha particles, have a much higher LET and produce densely spaced ionizations distributed among far fewer tracks to achieve the same dose. For low-LET tracks, the same basic concepts involving the interaction of multiple proximate breaks apply. However, since the average distance between high-LET tracks for a given dose is greater compared to that for low-LET tracks, high-LET track interaction is effectively eliminated for any dose that is likely to be used in an experimental setting. Thus, chromosome exchange formation for high-LET tracks is effectively confined to interactions of breaks caused by single-track action, which is in favor of a linear dose response.

The experimental dose-response curves shown in Fig. 13 do not align well with a linear-quadratic model. However, many experiments (*14, 29, 30*) and theories (*31*) support the assumption of a linear-quadratic model for CA. The main difference is that the doses used for these experiments are often an order of magnitude higher than those used in the current work. At low doses, the calculated CA yield is more difficult to obtain due to poor statistics. Furthermore, some CAs are also present in sham-irradiated cells (referred to as background). These background CAs have much more influence on the total CA yield at low doses than at high doses, because the CA yield increases with dose. Furthermore, there is a possibility of non-targeted effects at low dose, especially for high-LET ions. Overall, these contributing factors cause the results to deviate from the linear-quadratic model.

This code is largely based on the previous NASARTI work, which dates back several years. It is possible that a recalibration of the model using newer experimental data is necessary. It could also be useful to review some details included in the model such as DNA break complexity and different repair pathways.

CONCLUSIONS

In this work, the new simulation program RITCARD, which is inspired by the code NASARTI, was presented. RITCARD was developed using modern software engineering practices to enable future model advancements (i.e., mixed-field and dose-rate simulations) to be implemented more efficiently and reliably. Although RITCARD and NASARTI are based on the same fundamental theoretical framework, the numerical implementation is vastly different, with the new code (RITCARD) being more reliable, portable, efficient and well documented. By building this code, the structure and algorithms of NASARTI were followed as closely as possible. However, this program and RITRACKS include many improvements as well as new simulation capabilities. For instance, the RITRACKS program now allows multiple ion types to be simulated during irradiation. Amorphous tracks were replaced by stochastic tracks in our CA simulation models. RITCARD

Downloaded From: https://bioone.org/journals/Radiation-Research on 02 May 2024
Terms of Use: https://bioone.org/terms-of-use

is also built to include time dependence in the model, which will allow the study of dose-rate effects on CA in future work. RITCARD uses extensively C++ classes, which are well suited to model and manipulate real-life objects. Due to numerous changes, it was appropriate that a different name be used for this new code. The code is well structured, as shown by a low methods toxicity score. The changes are tracked using the GitLab environment, in accordance with modern software engineering standards. Thanks to its modular structure, the code can be easily modified to include new elements and improvements in the model, notably regarding breaks and repair mechanisms.

The programs were used to perform a systematic study of radiation-induced CA. The dose-response curves of the yields of CA were obtained for several ions of energies varying from 10 to 1,000 MeV/n. In general, the simulated dose-response curves are well approximated by a linear-quadratic model. The coefficient α of this curve appears to peak at approximately 100 keV/μm, suggesting relative biological effectiveness. This peak appears naturally in the calculations, without introducing additional assumptions or parameters in the model. This is very interesting because the model is essentially based on physical calculations. For instance, basically, the radiation-induced chromatin fiber damage is included in Eq. (3), with the voxel dose obtained from the track structure. The experimental data are in relatively good agreement with the simulation results at very low doses (0–0.1 Gy), but the simulation and experimental results diverge as dose increases beyond 0.1 Gy. Several possible explanations have been suggested in the Discussion. A recalibration and possibly a review of the repair kinetics, in which newer experimental data are considered, might be warranted. Thanks to the highly modular structure of RITCARD, it will be relatively easy to implement and test new repair kinetics models without interfering with other parts of the code.

This program will be very useful for the NASA Space Radiation Program. Further use of the code will include calculation of radiation-induced CA for mixed-field and chronic exposures, which are more representative of the GCR environment.

APPENDIX

Appendix 1: Files Generated

This appendix provides a description of the files generated by the program RITCARD, with examples (Figs. A1–A9). As counters in C++ usually start with 0 (not 1), many first elements in files are numbered with index 0.

RWIntersectionsBreaks.dat. This file (shown in Fig. A1) comprises information about the break locations.

FreeEnds.dat. This file (shown in Fig. A2) comprises information on the free ends.

FragmentsFE.dat. This file (shown in Fig. A3) contains information on the fragments comprising free ends.

FragmentsFESchema.dat. This file (shown in Fig. A4) schematically displays the fragments.

FreeEndPairs.dat. This long file (shown in Fig. A5) comprises all possible free end pairs in the system.

FreeEndPairsRepairs.dat. This file (shown in Fig. A6) is essentially identical to the file FreeEndPairs.dat, but comprising only the free end pairs that were repaired. All other free end pairs were discarded.

FragmentsSequence.dat. This important file file (shown in Fig. A7) contains the information about the fragment restitution after repair.

FragmentsSequenceSchema.dat. This file (shown in Fig. A8) displays the fragment sequence as well as the type of aberrations calculated. This is essentially the file FragmentsSequence.dat in schematic form.

FragmentsGroups.dat. The groups in this file (shown in Fig. A9) are used to classify aberrations.

No	Chromo	RWIndex	VoxelNo	xVox	yVox	zVox	Time	Break
0	0	129395	263	-21	68	224	5.4285e-14	1
1	0	129532	1158	-20	63	224	2.9469e-14	1
2	0	129643	1158	-20	63	224	2.9469e-14	1
3	18	38627	1258	102	117	20	5.4285e-14	1
4	23	47202	1319	102	112	21	5.1183e-14	1
5	23	68852	1345	101	146	21	6.6693e-14	1
6	24	8307	1306	-125	85	-148	3.8775e-14	1
7	28	44529	940	104	94	66	4.8081e-14	1

FIG. A1. RWIntersectionsBreaks.dat. This file comprises information about the break locations. Chromo = chromosome number (0 to 45); RWIndex = the random walk monomer index; VoxelNo = the number of the voxel; xVox, yVox and zVox = the spatial location of the voxel or monomer; Time = the creation time (s); and break = the presence of a break.

No	Fragm	Extr	Chromo	RWIndex	xVox	yVox	zVox	Time
0	0	1	0	129395	-21	68	224	5.4285e-14
1	1	0	0	129395	-21	68	224	5.4285e-14
2	1	1	0	129532	-20	63	224	2.9469e-14
3	2	0	0	129532	-20	63	224	2.9469e-14
4	2	1	0	129643	-20	63	224	2.9469e-14
5	3	0	0	129643	-20	63	224	2.9469e-14
6	4	1	18	38627	102	117	20	5.4285e-14
7	5	0	18	38627	102	117	20	5.4285e-14
8	6	1	23	47202	102	112	21	5.1183e-14
9	7	0	23	47202	102	112	21	5.1183e-14
10	7	1	23	68852	101	146	21	6.6693e-14
11	8	0	23	68852	101	146	21	6.6693e-14
12	9	1	24	8307	-125	85	-148	3.8775e-14
13	10	0	24	8307	-125	85	-148	3.8775e-14
14	11	1	28	44529	104	94	66	4.8081e-14
15	12	0	28	44529	104	94	66	4.8081e-14

FIG. A2. FreeEnds.dat. This file comprises information on the free ends. Since each break leads to two free ends, the number of lines is twice the number of lines in RWIntersectionBreaks.dat. No = the free end number; Fragm = the fragment number; Extr = the extremity (left = 0, right = 1); Chromo = chromosome number (0 to 45); RWIndex = the random walk monomer index; xVox, yVox and zVox = the spatial location of the voxel or monomer; Time = the creation time (s).

Downloaded From: https://bioone.org/journals/Radiation-Research on 02 May 2024
Terms of Use: https://bioone.org/terms-of-use

No	Chromo	RWInd1	RWInd2	Length	Tel1	Tel2	xVox1	yVox1	zVox1	xVox2	yVox2	zVox2	FrEnd1	FrEnd2	Time1	Time2
0	0	0	129395	129395	1	0	-295	141	124	-21	68	224	-1	0	0	5.4285e-14
1	0	129395	129532	137	0	0	-21	68	224	-20	63	224	1	2	5.4285e-14	2.9469e-14
2	0	129532	129643	111	0	0	-20	63	224	-20	63	224	3	4	2.9469e-14	2.9469e-14
3	0	129643	131500	1857	0	1	-20	63	224	-38	75	250	5	-1	2.9469e-14	0
4	18	0	38627	38627	1	0	131	234	-3	102	117	20	-1	6	0	5.4285e-14
5	18	38627	72000	33373	0	1	102	117	20	127	114	-54	7	-1	5.4285e-14	0
6	23	0	47202	47202	1	0	132	187	93	102	112	21	-1	8	0	5.1183e-14
7	23	47202	68852	21650	0	0	102	112	21	101	146	21	9	10	5.1183e-14	6.6693e-14
8	23	68852	71500	2648	0	1	101	146	21	130	123	-14	11	-1	6.6693e-14	0
9	24	0	8307	8307	1	0	-144	161	-169	-125	85	-148	-1	12	0	3.8775e-14
10	24	8307	57000	48693	0	1	-125	85	-148	-59	177	-306	13	-1	3.8775e-14	0
11	28	0	44529	44529	1	0	115	99	122	104	94	66	-1	14	0	4.8081e-14
12	28	44529	53000	8471	0	1	104	94	66	101	68	90	15	-1	4.8081e-14	0

FIG. A3. FragmentsFE.dat. This file contains information on the fragments comprising free ends. Chromo = is the chromosome number (0 to 45); RWInd1 and RWInd2 = the random walk monomer indices; Length = the length in monomer; Tel1 and Tel2 = presence or absence of a telomere; xVox1, yVox1, zVox1, xVox2, yVox2 and zVox2 = the spatial locations of the free ends; FrEnd1 and FrEnd2 = the free end number from the file FreeEnds.dat (–1 for telomeres); Time1 and Time2 = the creation times of the free ends (s; 0 for telomeres).

Downloaded From: https://bioone.org/journals/Radiation-Research on 02 May 2024
Terms of Use: https://bioone.org/terms-of-use

```
Fragments

Tel                          0
o>>>>>>>>>>C> 0>>>>>>>>>>>>>x

1                            2
x>>>>>>>>>>>>> 0>>>>>>>>>>>>>x

3                            4
x>>>>>>>>>>>>> 0>>>>>>>>>>>>>x

5                          Tel
x>>>>>>>>>>>>> 0>>>>>>>>>>>>>o

Tel                          6
o>>>>>>>>>>>>>18>>>>>>>>>>>>>x

7                          Tel
x>>>>>>>>>>C>18>>>>>>>>>>>>>o

Tel                          8
o>>>>>>>>>>C>23>>>>>>>>>>>>>x

9                           10
x>>>>>>>>>>>>>23>>>>>>>>>>>>>x

11                         Tel
x>>>>>>>>>>>>>23>>>>>>>>>>>>>o

Tel                         12
o>>>>>>>>>>>>>24>>>>>>>>>>>>>x

13                         Tel
x>>>>>>>>>>C>24>>>>>>>>>>>>>o

Tel                         14
o>>>>>>>>>>C>28>>>>>>>>>>>>>x

15                         Tel
x>>>>>>>>>>>>>28>>>>>>>>>>>>>o
```

FIG. A4. FragmentsFESchema.dat. This file displays schematically the fragments. The numbers on the first line indicate the index of the free end, or if it is a telomere (Tel). In the second line, ''o'' is a telomere, ''x'' is a free end, ''C'' indicates a centromere and ''>'' represents the direction of the DNA (3′–5′). The numbers in the second line indicate the chromosome number.

Downloaded From: https://bioone.org/journals/Radiation-Research on 02 May 2024
Terms of Use: https://bioone.org/terms-of-use

No	FreEn1	FreEn2	Frag1	Extr1	Frag2	Extr2	Chromo1	Chromo2	Proper	EuclD	ProbRep	Creat
0	0	1	0	1	1	0	0	0	1	0	0.00013885	5.4285e-14
1	0	2	0	1	1	1	0	0	0	5.09902	0.0197417	5.4285e-14
2	0	3	0	1	2	0	0	0	0	5.09902	0.0197417	5.4285e-14
3	0	4	0	1	2	1	0	0	0	5.09902	0.0197417	5.4285e-14
4	0	5	0	1	3	0	0	0	0	5.09902	0.0197417	5.4285e-14
5	0	6	0	1	4	1	0	18	0	243.2	2.8684e-15	5.4285e-14
							...					
116	12	15	9	1	12	0	24	28	0	313.557	8.94432e-24	4.8081e-14
117	13	14	10	0	11	1	24	28	0	313.557	8.94432e-24	4.8081e-14
118	13	15	10	0	12	0	24	28	0	313.557	8.94432e-24	4.8081e-14
119	14	15	11	1	12	0	28	28	1	0	0.00013885	4.8081e-14

FIG. A5. FreeEndPairs.dat. This long file comprises all possible free end pairs in the system. It has been truncated to fit in the page. The number of lines in this file is nFE(nFE-1)/2, where nFE is the number of free ends. In this example, since nFE = 16, the number of lines is 120. No = the free end pair index; FreEn1 and FreEn2 = the free end number (file FreeEnds.dat); Frag1 and Frag2 = the fragment number; Extr1 and Extr2 = the extremity of the fragment (left = 0, right = 1); Chromo1 and Chromo2 = the chromosome numbers; Proper indicates a proper rejoining; EuclD is the Euclidian distance between free ends in monomer units; ProbRep is the probability of rejoining during one time step; Creat = the creation time (s).

No	FreEn1	FreEn2	Frag1	Extr1	Frag2	Extr2	Chromo1	Chromo2	Proper	EuclD	ProbRep	Creat	Time_s
0	0	1	0	1	1	0	0	0	1	0	0.00013885	5.4285e-14	51.84
1	4	5	2	1	3	0	0	0	1	0	0.00013885	2.9469e-14	165.888
2	6	9	4	1	7	0	18	23	0	5.09902	0.0197417	5.4285e-14	217.728
3	14	15	11	1	12	0	28	28	1	0	0.00013885	4.8081e-14	238.464
4	2	3	1	1	2	0	0	0	1	0	0.00013885	2.9469e-14	285.12
5	10	11	7	1	8	0	23	23	1	0	0.00013885	6.6693e-14	311.04
6	12	13	9	1	10	0	24	24	1	0	0.00013885	3.8775e-14	352.512
7	7	8	5	0	6	1	18	23	0	5.09902	0.0197417	5.4285e-14	549.504

FIG. A6. FreeEndPairsRepairs.dat. This file is essentially identical to the file FreeEndPairs.dat, but comprises only the free end pairs that were repaired. All other free end pairs were discarded. Since a free end can be rejoined only once, a free end pair index can appear only once in the columns FreEn1 and FreEn2.

No	Type	FEnd1	Frag	FEnd2	FEnd1	Frag	FEnd2	FEnd1	Frag	FEnd2	FEnd1	Frag	FEnd2
0	0	-1	0	0	1	1	2	3	2	4	5	3	-1
1	5	-1	4	6	9	7	10	11	8	-1			
2	5	-1	6	8	7	5	-1						
3	0	-1	9	12	13	10	-1						
4	0	-1	11	14	15	12	-1						

FIG. A7. FragmentsSequence.dat. This important file contains the information about the fragment restitution after repair. No = the fragment sequence number; Type = CA type. The sequence reads FEnd1 – Frag – FEnd2 – FEnd1 – Frag – FEnd2 – …, indicating the first free end index, the fragment index and the second free end index. A free end with a value of –1 indicates the location of a telomere. Each junction FEnd2 – FEnd1 is associated with a repair in the file FreeEndPairsRepairs.dat. In this case, only one or two repairs are found on each sequence, corresponding to one line in this file. However, each repair contributes an additional fragment, which makes this file wider.

```
Group number: 0
-----------------------------------------------

Tel                      0 1                        2 3                        4 5                      Tel
o>>>>>>>>>>C> 0>>>>>>>>>>>>x x>>>>>>>>>>>> 0>>>>>>>>>>>>x x>>>>>>>>>>>> 0>>>>>>>>>>>>x x>>>>>>>>>>>> 0>>>>>>>>>>>>o     0       0       131500  Proper repair


Group number: 1
-----------------------------------------------

Tel                      6 9                       10 11                      Tel
o>>>>>>>>>>>>18>>>>>>>>>>>>x x>>>>>>>>>>>>23>>>>>>>>>>>>x x>>>>>>>>>>>>23>>>>>>>>>>>>o  1       1       62925           Exchange P1

Tel                      8 7                      Tel
o>>>>>>>>>>C>23>>>>>>>>>>>>x x>>>>>>>>>>C>18>>>>>>>>>>>>o       1       1       80575           Polycentric     Exchange P2


Group number: 2
-----------------------------------------------

Tel                     12 13                     Tel
o>>>>>>>>>>>>24>>>>>>>>>>>>x x>>>>>>>>>>C>24>>>>>>>>>>>>o       0       2       57000   Proper repair


Group number: 3
-----------------------------------------------

Tel                     14 15                     Tel
o>>>>>>>>>>C>28>>>>>>>>>>>>x x>>>>>>>>>>>>28>>>>>>>>>>>>o       0       3       53000   Proper repair
```

FIG. A8. FragmentsSequenceSchema.dat. This displays the fragment sequence as well as the type of aberrations calculated. This is essentially the file FragmentsSequence.dat in schematic form. The consecutive numbers on the first lines correspond to repairs. On the right side of the fragment sequence are the number of improper rejoinings, the fragment group in which they belong, the fragment length in monomer units and the type of aberration.

Downloaded From: https://bioone.org/journals/Radiation-Research on 02 May 2024
Terms of Use: https://bioone.org/terms-of-use

```
No      Chromo          Sequences
0       {0  }           {0  }
1       {18 23  }       {1 2  }
2       {24  }          {3  }
3       {28  }          {4  }
```

FIG. A9. FragmentsGroups.dat. The groups in this file are used to classify aberrations. No = the group number; Chromo = the chromosome material present in this group; and Sequences = the sequence numbers in the file FragmentSequence.dat. A group is the sequence containing material originating from one chromosome. The groups are necessarily disjoints, i.e., two groups should be merged if they contain material from one given chromosome.

ACKNOWLEDGMENTS

This work was supported by NASA Space Radiation Program (grant no. NNX16AR97G to MH), NASA Human Health and Performance Contract (HHPC; no. NNJ15HK11B), and TAMU Chancellor's Research Initiative, Texas A&M University.

Received: September 23, 2018; accepted: May 28, 2019; published online: July 11, 2019

REFERENCES

1. Saganti PB, Cucinotta FA, Wilson JW, Simonsen LC, Zeitlin C Radiation climate map for analyzing risks to astronauts on the Mars surface from galactic cosmic rays. Space Sci Rev 2004; 110:143–56.
2. Benton ER, Benton EV. Space radiation dosimetry in low-Earth orbit and beyond. Nucl Instr Meth Phys Res B: Beam Interactions with Materials and Atoms 2001; 184:255–94.
3. Cucinotta FA, Durante M Cancer risk from exposure to galactic cosmic rays: implications for space exploration by human beings. Lancet Oncol 2006; 7:431–5.
4. Bonassi S, Norppa H, Ceppi M, Stromberg U, Vermeulen R, Znaor A, et al. Chromosomal aberration frequency in lymphocytes predicts the risk of cancer: results from a pooled cohort study of 22,358 subjects in 11 countries. Carcinogenesis 2008; 29:1178–83.
5. Cao J, Zhang J, Wang Y, Du LQ, Xu C, Wang Q, et al. Cytogenetic abnormalities in lymphocytes from victims exposed to cobalt-60 radiation. Int J Molec Sci 2013; 14:17525–35.
6. Kodama Y, Pawel D, Nakamura N, Preston D, Honda T, Itoh M, et al. Stable chromosome aberrations in atomic bomb survivors: results from 25 years of investigation. Radiat Res 2001; 156(4):337–46.
7. George K, Durante M, Willingham V, Wu H, Yang T, Cucinotta FA. Biological effectiveness of accelerated particles for the induction of chromosome damage measured in metaphase and interphase human lymphocytes. Radiat Res 2003; 160:425–35.
8. Ponomarev AL, George K, Cucinotta FA. Computational model of chromosome aberration yield induced by high- and low-LET radiation exposures. Radiat Res 2012; 177:727–37.
9. Ponomarev AL, George K, Cucinotta FA. Generalized time-dependent model of radiation-induced chromosomal aberrations in normal and repair-deficient human cells. Radiat Res 2014; 181:284–92.
10. McMahon SJ, Schuemann J, Paganetti H, Prise K Mechanistic modelling of DNA repair and cellular survival following radiation-induced DNA damage. Sci Reports 2016; 6:32290.
11. McMahon SJ, McNarama AL, Schuemann J, Paganetti H, Prise K A general mechanistic model enables predictions of the biological effectiveness of different qualities of radiation. Sci Reports 2017; 7:10790.
12. George KA, Hada M, Jackson LJ, Elliott T, Kawata T, Pluth JM, et al. Dose response of gamma-rays and iron nuclei for induction of chromosomal aberrations in normal and repair-deficient cell lines. Radiat Res 2009; 171:752–63.
13. Hada M, Chappell LJ, Wang M, George K, Cucinotta FA. Induction of chromosomal aberrations at fluences of less than one HZE particle per cell nucleus. Radiat Res 2014; 182:368–79.
14. Loucas BD, Durante M, Bailey SM, Cornforth MN. Chromosome damage in human cells by gamma rays, alpha particles and heavy ions: track interactions in basic dose-response relationships. Radiat Res 2012; 179:9–20.
15. Bailey SM, Cornforth MN. Telomeres and DNA double-strand breaks: ever the twain shall meet? Cell Mol Life Sci 2007; 64:2956–64.
16. Plante I, Cucinotta FA. Multiple CPU computing: the example of the code RITRACKS. International Meeting on Computational Intelligence Methods for Bioinformatics and Biostatistics. Berlin, Heidelberg: Springer; 2012. p. 12–25.
17. Ponomarev AL, Sach RK. Polymer chromosome models and Monte Carlo simulations of radiation breaking DNA. Bioinformatics 1999; 15:957–64.
18. Ponomarev AL, Sach RK. Radiation breakage of DNA: a model based on random-walk chromatin structure. J Math Biol 2001; 43:356–76.
19. Ponomarev AL, Cucinotta FA. Chromatin loops are responsible for higher counts of small DNA fragments induced by high-LET radiation, while chromosomal domains do not affect the fragment sizes. Int J Radiat Biol 2006; 82:293–305.
20. Plante I, Cucinotta FA. Monte-Carlo simulation of ionizing radiation tracks. In: Mode CJ, editor. Applications of Monte Carlo methods in biology, medicine and other fields of science. London: InTech; 2011. p. 2476.
21. Plante I, Ponomarev AL, Cucinotta FA. Calculation of the energy deposition in nanovolumes by protons and HZE particles: geometric patterns of initial distributions of DNA repair foci. Phys Med Biol 2013; 58:6393–405.
22. Turner J. Atoms, radiation and radiation protection. 3rd. ed. New York: Wiley; 2007.
23. Meesungnoen J, Jay-Gerin J-P, Filali-Mouhim A, Mankhetkorn S Low-energy electron penetration range in liquid water. Radiat Res 2002; 158:657–60.
24. Savage JRK. Classification and relationships of induced chromosomal structural changes. J Med Genetics 1975; 12:103–22.
25. Yannone SM, Roy S, Chan DW, Murphy MB, Huang S, Campisi J, et al. Werner syndrome protein is regulated and phosphorylated by DNA-dependent protein kinase. J Biol Chem 2001; 276:38242–8.
26. Hada M, Huff JL, Patel Z, Kawata T, Pluth JM, George KA, et al. AT cells are not radiosensitive for chromosomal exchanges at low dose. Mutat Res 2011; 716:76–83.
27. Savage RK, Simpson PJ. On scoring of FISH-''painted'' chromosome-type exchange aberrations. Mutat Res 1994; 307:345–53.
28. Lucas JN, Poggensee M, Straume T The persistence of chromosome translocations in a radiation worker accidentally exposed to tritium. Cytogenet Cell Genet 1993; 60:225–56.
29. George K, Hada M, Chappell L, Cucinotta FA. Biological effectiveness of accelerated particles for the induction of chromosome damage: Track structure effects. Radiat Res 2013; 180:25–33.
30. Wu H, Durante M, George K, Yang TC. Induction of chromosome aberrations in human cells by charged particles. Radiat Res 1997; 148:S102–7.
31. Kellerer AM, Rossi HH. The theory of dual radiation action. Curr Top Radiat Res Q 1974; 85–158.

Downloaded From: https://bioone.org/journals/Radiation-Research on 02 May 2024
Terms of Use: https://bioone.org/terms-of-use